HIGH-RESOLUTION IMAGING BASED ON COHERENT PROCESSING FOR DISTRIBUTED MULTI-BAND RADAR DATA

Feiyang He[*] and Xiaojian Xu

School of Electronic and Information Engineering, Beihang University, Beijing 100191, China

Abstract—A coherent processing method for subband signals of distributed multi-band radar data is proposed and tested. The method uses de-noising cross-correlation (DNCC) algorithm and statistical method to obtain phase incoherent parameters (ICP) between subband signals. After compensating the phase ICP, a coherence function is defined and combined with statistical method to find amplitude ICP. Finally, data fusion method via two-dimensional gapped-data state space approach (2-D GSSA) is applied to subband signals and high-resolution imaging of target is achieved. The advantage of this method lies in that it can be used to process subband signals of different bandwidth and different gaps between them. To validate our work, electromagnetic calculation target and real target measured in microwave chamber are analyzed and used for testing different mutual-coherence and data fusion algorithms. Experimental results demonstrate the superiority of the proposed method over previous approaches in terms of improved imaging quality and performance.

1. INTRODUCTION

Nowadays, modern wideband radar systems have the capability of obtaining more features of the targets to carry out real-time discrimination and target identification. This capability is primarily the result of target resolution improvement. Ultra-wideband (UWB) imaging is a good way to improve target range resolution. However, due to specific engineering or technology constraints, it is usually difficult for a single radar system to operate over a very large bandwidth. As the next generation radar, distributed radar has

great promise for various sensing applications. Distributed multi-band
radar can be used to synthesize large bandwidth for achieving high-
resolution radar imagery of many targets [1–5]. Actually, there are two
challenges for this application. First, in real radar applications, the
relative bandwidth of radar is limited by its center frequency and it is
about of 10% of the center frequency, the subbands may have different
bandwidth and large bandwidth gaps. Accurate coherent processing
for these subbands must be performed at first. Second, different data
gaps between subbands should be filled to form the final high-resolution
images.

Among the existing coherent processing methods, coherence
function [1] is used to acquire incoherent parameters (ICP), but large
extrapolation errors may occur, and it is easily trapped in local
optimization. Pole rotation method [3, 4] is used to obtain phase ICP;
however, it is required that all the subbands have the same bandwidth.
In [5], a data based coherent compensation method is used for coherent
processing, but it is easily influenced by noise due to lack of de-noising
process. For the data fusion methods, the available algorithms include
nonparametric spectrum estimation [6–10], the parametric spectrum
estimation method [1, 12, 13] and p-norm regularization method [14].
In [6], Burg algorithm is used to find the linear prediction parameters
and a iterative procedure is used to improve the estimation of the
parameters and the extrapolation of the data, but the gaps between
subbands can not be too large. In [7, 8], minimum weighted norm
(MWN) method is used for optimizing one-dimensional (1-D) aperture
extrapolation, but it may not suitable for multi-band data with few
data samples and large gaps. In [9–11], the method called gapped-
data APES (GAPES) is used for data fusion, which is based on an
interpolation of the gapped data under certain constraints. However,
the computational burden is a problem for real-time processing.
Reference [1] uses the all-pole model and the root-MUSIC for model
parameter estimation. In [12, 13], an 1-D gapped-data state space
approach (1-D GSSA) is used to estimate parameters of complex
exponential (CE) model for gaps data estimation. In [14, 15], the Lp-
norm regularization method with $0 < p < 1$ is applied for partial-
aperture and sparse band imaging, where the choice of p remains an
open problem. With a large number of missing samples, simulations
have shown that the regularization method may be unable to obtain a
satisfying outcome.

In this paper, a coherent processing technique is proposed to
process multi-band data of different bandwidth and different gaps
between subbands. We use de-noising cross-correlation (DNCC)
algorithm and statistical method to obtain estimation of phase ICP

along every azimuth.   A coherence function is used to estimate
amplitude ICP after phase ICP is compensated and statistical method
is used to obtain optimal amplitude ICP. Finally, data fusion method
via two-dimensional gapped-data state space approach (2-D GSSA) is
applied to subbands and high-resolution imaging is achieved to enhance
the capability of target discrimination and identification.

2. DISTRIBUTED MULTI-BAND RADAR

In this section, we will describe the general imaging geometry for
distributed collocated multi-band radar.

2.1. Distributed Collocated Radar Imaging Geometry

Figure 1 illustrates a scenario in which three collocated radars are
interrogating an unknown target in the aerospace, simultaneously.
Each radar can produce a 'snapshot' image by using range-Doppler
algorithm when target rotates a small angle [16].   As is shown in
Figure 1, the radars operate at the different frequency band and share
the same target aperture. Here, different subband signals mean the
signals transmitted by different collocated radars. The radars operate
at different center frequency with different bandwidth. For instance,
S-band centered at $3\,\text{GHz}$ with $300\,\text{MHz}$ bandwidth, C-band data
centered at $6\,\text{GHz}$ with $600\,\text{MHz}$ bandwidth, X-band data centered at
$10\,\text{GHz}$ with $1\,\text{GHz}$ bandwidth. For application considered here, the
target motion in the aerospace is determined by two basis components:
a trajectory motion, generally characterized by the motion of the center
of gravity of the target, and a localized motion about center of rotation
of the body. In this paper, we assume that the trajectory motion is
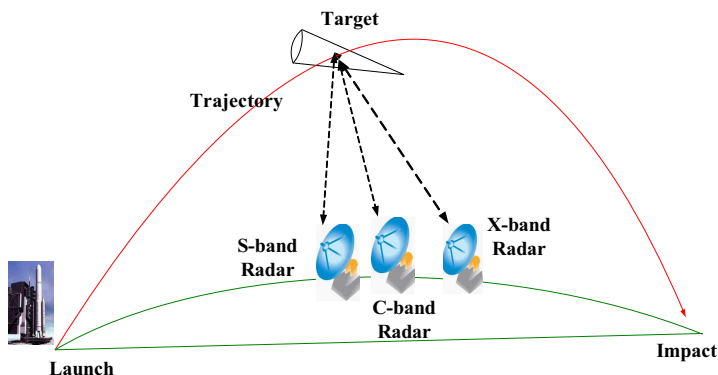
Figure 1. Imaging geometry.

compensated and the radar pulses are range aligned such that body motion is centered about the body axis of rotation. As we known, subband data coherence is essential before coherent combination of the data, mutual-coherence errors occur because of range-estimation bias and radar amplitude gain bias. This paper studies the methods for mutually cohering the subband radar data. The goal is to obtain the best-possible image from multi-sensor data, so that the resultant image can be fed into a target characterization process for full characterization.

2.2. Signal Model

The received echo signal $y(f, \vartheta)$ of a target at frequency f and aspect angle ϑ can be expressed as follows [17]:

$$y(f, \vartheta) = \sum_{i=1}^{P} \sigma_i e^{-j\frac{4\pi f}{c}(x_i \cos \vartheta + y_i \sin \vartheta)} + v(f, \vartheta) \qquad (1)$$

where P is the number of scattering centers on the target, σ_i the amplitude of the i-th scattering center, and $(x_i; y_i)$ the position of the i-th scattering center in the spatial domain. v is the additive white Gaussian noise (AWGN) and c the speed of light.

Equation (1) illustrates that the phase of the received signal varies as a function of aspect angle. When the target rotates, the received radar data is collected in polar format. Although such data may be collected at uniformly spaced frequency steps and rotation angle positions, the samples are nonuniformly spaced in the spatial frequency domain. The results is that two-dimensional Fourier transform to target-space reflectivity results in unfocused images for the large rotation angles. An optional method for inverse synthetic aperture radar (ISAR) imaging is the natural double integral imaging method

$$I(x, y) = \iint\limits_{\vartheta f} y(f, \vartheta) e^{j\frac{4\pi f}{c}(x \cos \vartheta + y \sin \vartheta)} df d\vartheta \qquad (2)$$

Although the natural integration method provides better resolved images in range and azimuth domains for large rotation angles, the main drawback is the considerable computation time in evaluating the ISAR integral.

To improve the computation efficiency, we should make full use of fast Fourier transform (FFT) for ISAR imaging. For 'snapshot' imaging, i.e., small rotational angle case, FFT can be used to form ISAR image of the target. For large rotation angle case, the received backscattering data uniformly sampled in the frequency-aspect domain

does not correspond to the uniformly sampled data in the spatial frequency domain, so the polar formatting algorithm (PFA) [24] should be used that allows us to retain the computational advantage of the 2-D FFT exploited in the imaging algorithm.

3. SUBBAND DATA COHERENT PROCESSING AND DATA FUSION

Figure 2 shows the diagram of data processing flow. Coherent processing between subbands data must be carried on first. In this step, it estimates and compensates the phase and amplitude ICP between subband data. After that, subband data can be combined to form large bandwidth data. In the last step, 2-D FFT is used to form ISAR image of the target.
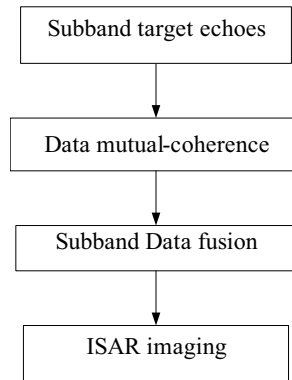

Figure 2. The data processing flow chart.

3.1. Coherent Processing of Subband Data

According to the configuration in 2.1, the target is illuminated by three collocated radars which operate at different subbands with different bandwidth, simultaneously. The subband with largest bandwidth, i.e., X-band data is used to be a reference. Coherent processing is applied to compensate for the lack of mutual coherence between the reference radar and others. The data mutual-coherence procedure between subband data is shown in Figure 3. After optimal phase and amplitude ICP are estimated and compensated, subband data can be combined to form a large bandwidth data.

Without loss of generality, we consider mutual incoherence between S-band data and X-band data. The method can also be
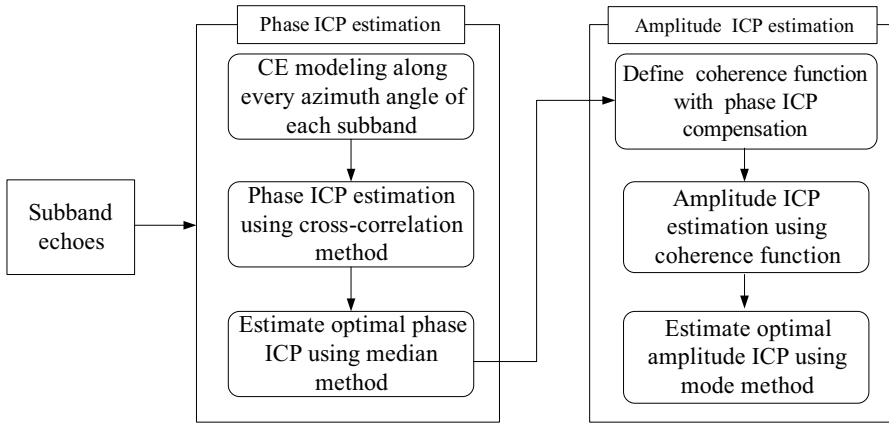
Figure 3. Data mutual-coherence.

extended to arbitrary subbands data mutual-coherence. Here, we treat
X-band radar as a reference one. The radar returns from S-band data
and X-band data at a certain azimuth can be written as [2]

$$y_{nS}(k) = Ay(k)e^{j(k-1)\phi} + v_1(k); \quad k = 1, 2, \ldots, N_1 \qquad (3)$$
$$y_{nX}(k) = y(k) + v_2(k); \quad k = N - N_2 + 1, \ldots, N \qquad (4)$$

where $y(k)$ denotes fullband radar return without noise; $v_1(k)$ and
$v_2(k)$ are AWGN; A and ϕ are amplitude and phase ICP, respectively;
N denotes frequency samples number of fullband. S-band data
contains N_1 frequency data samples, and reference one contains N_2
frequency data samples. Data mutual-coherence between them is as
follows.

The radar returns of two subband data can be modeled by CE
model [18, 19]

$$y(k) = \sum_{i=1}^{p} a_i e^{-\left(\alpha_i + j4\pi \frac{r_i}{c}\right)f_k} \qquad (5)$$

where a_i and α_i are respectively the amplitude and dispersion factor
of ith scattering center, and r_i the relative range and c the speed
of light. The frequency vector f_k is specified in terms of the carrier
frequency f_c as $f_k = f_c + (k-1)\Delta f$, where Δf is frequency step. p
denotes the number of the scattering centers. Order selection method
is used to estimate p, here, we use two methods combined together
to estimate it, one is singular value decomposition (SVD) method
through selecting proper threshold, the other one is information
criterion [20, 21]. SSA [18] is used to estimate those parameters in (5)

except p, and subband signals after de-noising are obtained as $y_S(k)$ and $y_X(k)$. If we consider that the target characteristic at certain aspects is similar according to each radar.

$$y_X(k) = \frac{1}{A} y_S(k) e^{-j(k-1)\phi} \tag{6}$$

We compute N_c point inverse fast Fourier transform (IFFT) of $y_S(k)$ and $y_X(k)$ to obtain $Y_S(n)$ and $Y_X(n)$, so the correlation function can be obtained as $R(n) = Y_X(n) \otimes Y_S^*(-n)$, where $\otimes$ denotes circular convolution. * denotes conjugate transpose. The function can also be rewritten as

$$R(n) = \frac{1}{N_c} \sum_{k=1}^{N_c} y_X(k) y_S^*(k) e^{j\frac{2\pi}{N_c}(k-1)(n-1)}; \quad n = 1, \dots, N_c \tag{7}$$

The formula after substituting (6) to (7) has the form

$$R(n) = \frac{1}{A \cdot N_c} \sum_{k=1}^{N_c} |y_S(k)|^2 \, e^{j\frac{2\pi}{N_c}(k-1)\left(n-1-\frac{N_c}{2\pi}\phi\right)}; \quad n = 1, \dots, N_c \tag{8}$$

Equation (8) indicates that the maximum of the function can be achieved when $n = N_c\phi/2\pi + 1$, so $\phi = 2\pi(n-1)/N_c$. If the radar echo contains N_a pair of aspects, the final estimation of phase ICP can be obtained as $\phi_{opt} = \underset{q=1,\dots,N_a}{\text{median}} \{\phi_q\}$, where 'median' denotes computing median of the array.

A coherence function is defined, and the S-band data is compensated with the optimal phase ICP

$$C_F = \sum_{k=1}^{N_1} \left| \frac{1}{A} y_S(k) e^{-j(k-1)\phi_{opt}} - y_X(k) \right|^2 \tag{9}$$

Optimization is performed to estimate amplitude ICP. The optimal estimation of the amplitude ICP can be obtained as $A_{opt} = \underset{q=1,\dots,N_a}{\text{mode}} \{A_q\}$, where 'mode' denotes computation of the most frequent values in array.

3.2. Subband Data Fusion

After all the ICP corresponding to S-band data and C-band data are estimated and compensated with X-band data, data fusion by using 2-D GSSA can be carried on mutually cohered subband data. Figure 4 shows flow chart of subband data fusion.
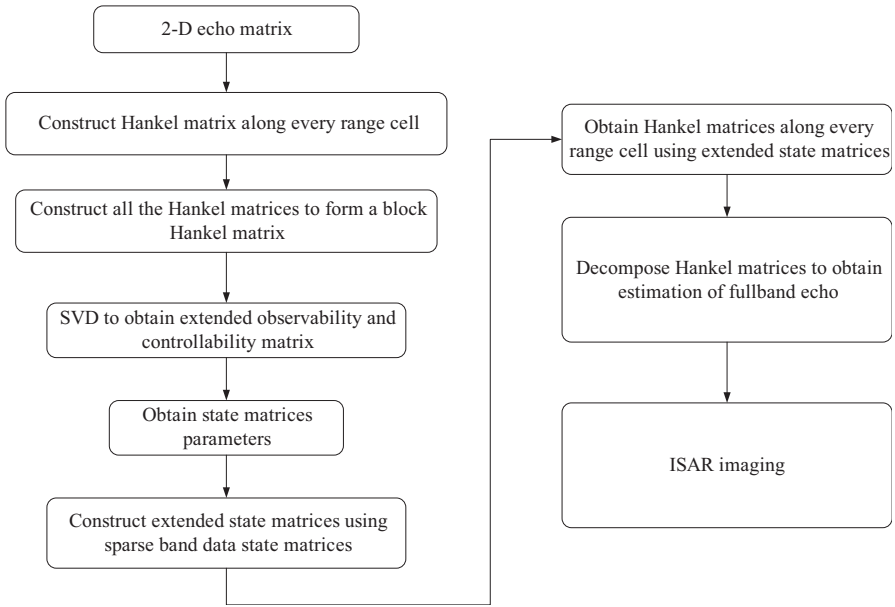
Figure 4. Flow chart of subband data fusion.

For linear imaging, formula (1) can be written as 2-D data samples $y(m, n)$ [22] that comprise P scattering centers corrupted with white Gaussian noise $v(m, n)$

$$y(m, n) = \sum_{i=1}^{P} a_i s_i^m q_i^n + v(m, n) \tag{10}$$

where a_i refers to the complex amplitude associated with the of ith scattering center with pole pair (s_i, p_i). We assume that the length of S-band, C-band and X-band are N_1, N_2 and N_3, respectively. The length of data gaps between them are N_{g1} and N_{g2}, respectively. The set of three subband data may be written as

$$\mathbf{Y}_{bS} = \begin{bmatrix} y(1,1) & y(1,2) & \dots & y(1, N_1) \\ y(2,1) & y(2,2) & \dots & y(2, N_1) \\ \vdots & \vdots & \vdots & \vdots \\ y(M,1) & y(M,2) & \dots & y(M, N_1) \end{bmatrix} \tag{11}$$

$$\mathbf{Y}_{bC} = \begin{bmatrix} y(1, N_{g1} + N_1 + 1) & y(1, N_{g1} + N_1 + 2) & \dots \\ y(2, N_{g1} + N_1 + 1) & y(2, N_{g1} + N_1 + 2) & \dots \\ \vdots & \vdots & \vdots \\ y(M, N_{g1} + N_1 + 1) & y(M, N_{g1} + N_1 + 2) & \dots \end{bmatrix}$$

$$\left.\begin{matrix} y(1, N_{g1} + N_1 + N_2) \\ y(2, N_{g1} + N_1 + N_2) \\ \vdots \\ y(M, N_{g1} + N_1 + N_2) \end{matrix}\right] \tag{12}$$

$$\mathbf{Y}_{bX} = \begin{bmatrix} y(1, N-N_3+1) & y(1, N-N_3+2) & \dots & y(1, N) \\ y(2, N-N_3+1) & y(2, N-N_3+2) & \dots & y(2, N) \\ \vdots & \vdots & \vdots & \vdots \\ y(M, N-N_3+1) & y(M, N-N_3+2) & \dots & y(M, N) \end{bmatrix} \tag{13}$$

where M denotes the number of azimuth samples, $\mathbf{Y}_{bS}$ the S-band data, $\mathbf{Y}_{bC}$ the C-band data, and $\mathbf{Y}_{bX}$ the X-band data.

The state matrices $(\mathbf{A}_{cj}, \mathbf{B}_{cj}, \mathbf{C}_{cj})$ and column enhanced matrices $\mathbf{H}_{bj}^{col}$ can be obtained from two dimensional data sets [22], where $j = S, C, X$. The extended state matrices are constructed as follows

$$\begin{aligned} \mathbf{A} &= blkdiag(\mathbf{A}_{cS} \quad \mathbf{A}_{cC} \quad \mathbf{A}_{cX}) \\ \mathbf{B} &= [\mathbf{B}_{cS} \quad \mathbf{B}_{cC} \quad \mathbf{B}_{cX}]^{\mathrm{T}} \\ \mathbf{C} &= \left[\mathbf{H}_{bS}^{col} \quad \mathbf{H}_{bC}^{col} \quad \mathbf{H}_{bX}^{col}\right] \tilde{\Gamma}_N^* \left(\tilde{\Gamma}_N \tilde{\Gamma}_N^*\right)^{-1} \end{aligned} \tag{14}$$

where $\tilde{\Gamma}_N = [\mathbf{B} \quad \dots \quad \mathbf{A}^{N_1-1}\mathbf{B}, \quad \dots \quad , \mathbf{A}^{N-N_3}\mathbf{B} \quad \dots \quad \mathbf{A}^{N-1}\mathbf{B}]$, *blkdiag* denotes the block diagonal matrix. The Hankel matrices along every range cells can be expressed as

$$\mathbf{H}_n^{col} = \mathbf{C}\mathbf{A}^{n-1}\mathbf{B}; \quad n = 1, \dots, N \tag{15}$$

where N denotes frequency number of fullband samples. We decompose the Hankel matrices along every column to retrieve the estimation of range cell data, then, the data along every column can be deduced as

$$\mathbf{Y}_{eb}(:, n) = \left[\mathbf{H}_n^{col}(1:d_r-1, 1) \quad \mathbf{H}_n^{col}(d_r, :)^{\mathrm{T}} \right]^T; \quad n = 1, \dots, N \tag{16}$$

where d_r denotes the dimension of row of $\mathbf{H}_n^{col}$.

The final ISAR image of radar echo with subband data fusion can be generated by using 2-D FFT method, and improved ISAR images can be obtained.

4. EXPERIMENTAL RESULTS

In this section, two examples are presented to demonstrate the effectiveness and superiority of the proposed method.

4.1. Numerical Simulation Using Electromagnetic Calculation Target

In the first example, the proposed method is applied to a target calculated from physical optics (PO) and equivalent edge current (EEC) [23]. Figure 5 shows the shape and geometry of the target. The target model is a blunt nosed cone-cylinder-frustum (BNCCF) target. As we can see from Figure 5(a), the target is composed of three parts. The first part is a blunt nosed cone which has a sphere tip with a radius of 51 mm. The second part is a cylinder connecting with the first part and the third part. The third part is a frustum. The total length of the target is 1400 mm. The joint of cone and cylinder is located 692 mm from the target base. The joint of cylinder and frustum is located 92 mm from the target base. The other parameters such as diameter of the cylinder and target base are shown in Figure 5(b).


(a)

(b)
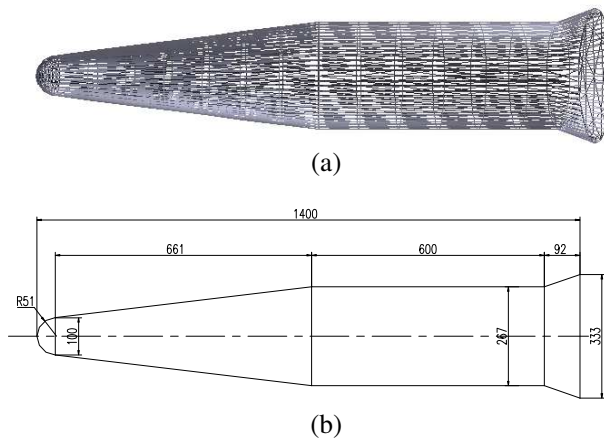
Figure 5. The shape and geometry of the BNCCF target. (a) The shape of the target. (b) The geometry of the target.

The primary aims of our experiment are to verify the proposed processing method for the distributed multi-band radar data to obtain high-resolution images of rigid targets in the aerospace. Calculations were taken from 2 to 20 GHz in 20 MHz increments, HH polarization. The target viewing angles, relative to nose-on, ranged from $-180°$ to $180°$ in $0.25°$ increments.

4.1.1. Comparison of Pole Rotation and DNCC Method

In this section, we investigate the performance of pole rotation [1] and DNCC method for estimating phase ICP. We consider two cases:

case 1, the subband $3 \sim 3.3\,\text{GHz}$ and $8 \sim 9\,\text{GHz}$ are mutually incoherent; case 2, the subband $13 \sim 14\,\text{GHz}$ and $16 \sim 17\,\text{GHz}$ are mutually incoherent. The target viewing angle is $5°$ and lower subband is modulated by phase bias $60°$ for two cases. AWGN is added to subband signals. The simulation number of Monte Carlo is 1000. Figure 6 shows the comparison of pole rotation and DNCC method. Note that the phase ICP estimation from DNCC method is more reliable than pole rotation method in all SNR circumstances.
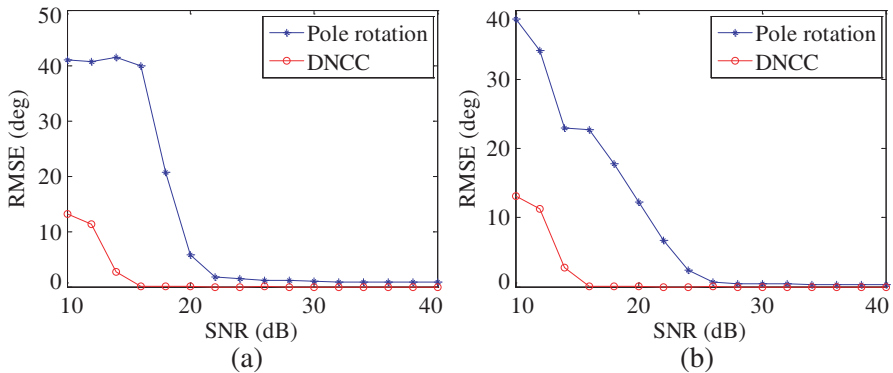
Figure 6. Comparison of phase ICP estimation methods. (a) Case 1. (b) Case 2.
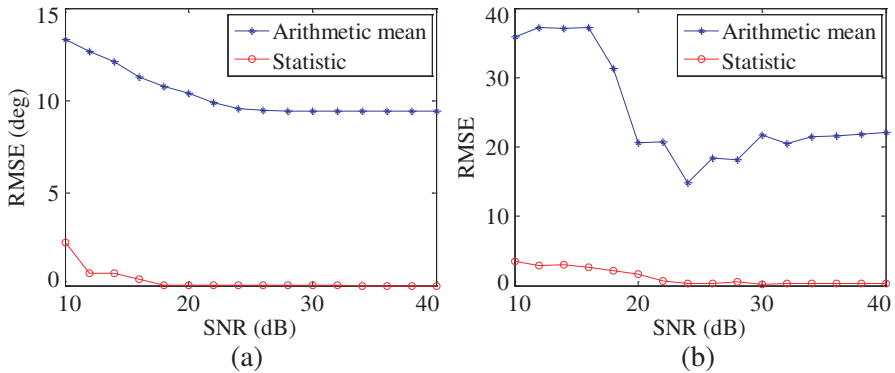
4.1.2. The Statistical Method for ICP Estimation

To obtain optimal phase ICP, statistical method is used in dwell time. Subband data used for simulation are from $4 \sim 5\,\text{GHz}$ and $7 \sim 8\,\text{GHz}$, respectively. The cumulative angle is from $0 \sim 10°$. To simulate the amplitude and phase incoherence between subband data, the lower subband data is modulated by a gain of 5 and phase bias of $45°$. AWGN is added to subband signals. The simulation number of Monte Carlo is 1000.

Figure 7 shows the root mean squared errors (RMSE) of phase and amplitude ICP estimation derived by statistical method and arithmetic mean method. It is seen that the proposed statistical method has better performance over arithmetic mean method.

4.1.3. Imaging Results of BNCCF Target

In order to simulate the real-world situation, we assume that there are three collocated radars which operate at S-band ($3 \sim 3.3\,\text{GHz}$), C-band ($5.7 \sim 6.3\,\text{GHz}$) and X-band ($8 \sim 9\,\text{GHz}$), respectively. The

Figure 7. Comparison of ICP estimation by arithmetic mean and statistical methods. (a) Phase ICP estimation. (b) Amplitude ICP estimation.

target is illuminated by these radars simultaneously and the target viewing angle ranging from $-3°$ to $3°$. The bandwidth of these radars are 300 MHz, 600 MHz, 1 GHz, respectively and all these radars are mutually incoherent. To simulate the amplitude and phase incoherence between the subbands, X-band is treated as a reference subband, S-band signals are modulated by a gain of 5 and phase bias $\pi/3$, C-band signals are modulated by a gain of 3 and phase bias $\pi/4$. Signal noise ratio (SNR) is set to be 20 dB.

Figures 8(a)–(c) depict ISAR images of these subbands by using two-dimensional (2-D) FFT, respectively. The resolution of these images are too coarse, especially the S-band data. They do not explicitly resolve the subtle features of the target. The full band data image is shown in Figure 8(d), which shows the target features including target base, joint of cylinder & frustum, joint of cone & cylinder and sphere tip. Compared to Figure 8(d), Figure 8(e) shows the image results by using 2-D GSSA without mutual-coherence, which can not show the correct distribution of scattering centers. As is known, mutual-coherence must be done before data fusion, Figures 8(f)–(i) compare different fusion algorithms after mutual-coherence processing. Figure 8(f) shows the result of GAPES, as we can see, the method can not improve range resolution and show subtle feature of the target, whereas induces grating lobes. Figures 8(g)–(h) show the results of 1-D GSSA and 1-D SSA combined with MWN, respectively. They can also improve the range resolution of sphere tip and target base, but lose the information of middle joints which is because the data is too sparse. By using 2-D GSSA, we can obtain all the subtle information about the target as shown in Figure 8(i), which

shows high fidelity comparable to Figure 8(d).

In real-time imaging applications, time cost is a key point for evaluating algorithm performance. After mutual-coherence processing, we compare the time cost of different data fusion algorithms. The numerical simulation experiments were conducted in the same personal computer and the simulation condition is as above. The time cost is as follows: 1-D GSSA is 0.8699 s, 1-D SSA+MWN is 1.9674 s, GAPES is 431.6062 s and 2-D SSA is 3.1126 s. From above analysis, 1-D SSA and
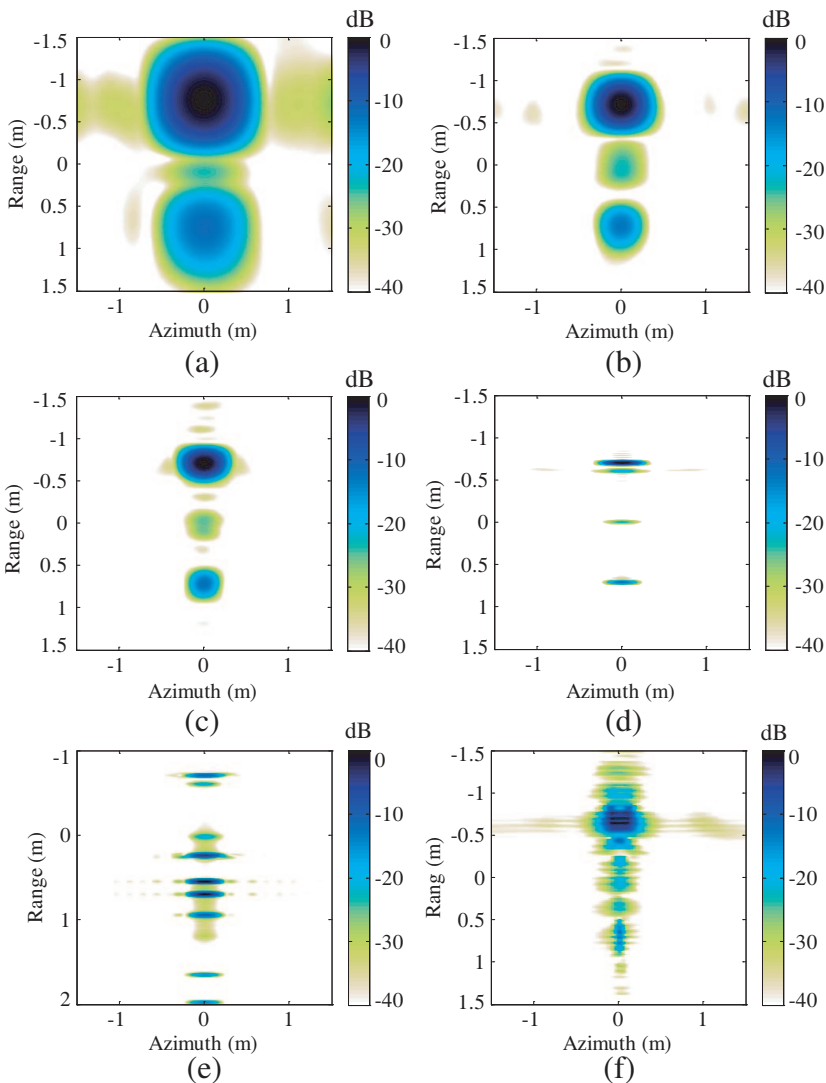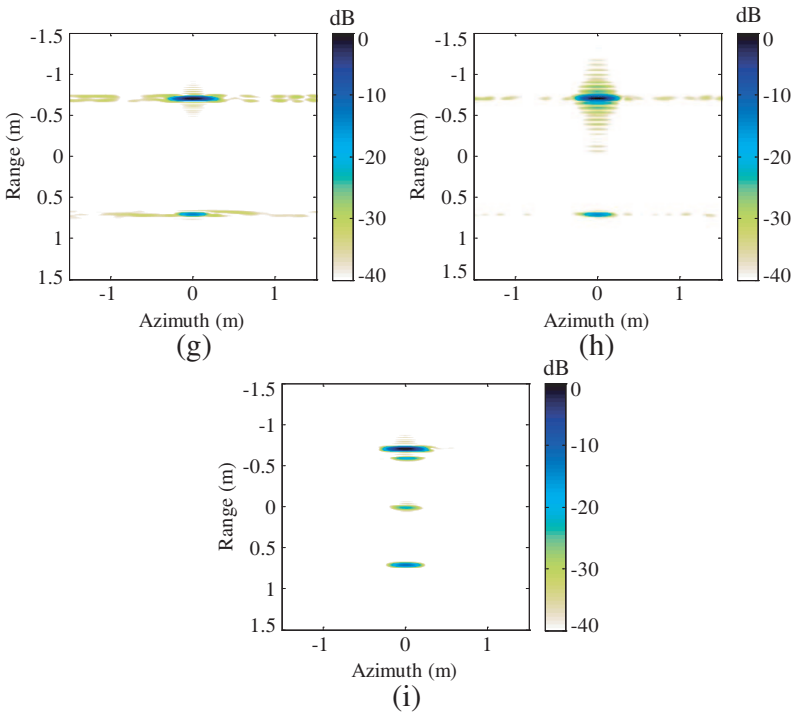
Figure 8. Comparison of 2-D radar images. (a) Subband (3 ∼ 3.3 GHz). (b) Subband (5.7 ∼ 6.3 GHz). (c) Subband (8 ∼ 9 GHz). (d) Full band (3 ∼ 9 GHz). (e) 2-D GSSA without mutual-coherence. (f) GAPES after mutual-coherence. (g) 1-D GSSA after mutual-coherence. (h) 1-D GSSA+MWN after mutual-coherence. (i) 2-D GSSA after mutual-coherence.

1-D SSA+MWN cost less time, but they may lose important scattering centers information and can not show subtle feature of the target. The time cost of GAPES is huge, so it's not suitable for real-time processing. 2-D GSSA supplies the best imaging outcome and the time cost is reasonable for the imaging applications.

4.2. Real Data Imaging Results

In this section, the proposed method is applied to a target measured from microwave chamber. Figure 9 shows the optical picture and geometry of the target. The target model is a blunt nosed cone-cylinder target. As we can see from Figure 9(a), the target is composed of three parts. The first part is a blunt nosed cone which has a sphere tip with a

radius of 22 mm and a piece of foil. The second part is a frustum, which connected the first and third parts. The total length of the target is 1200 mm. The joint A is located 930 mm from the target base. The joint B is located 430 mm from the target base. The other parameters are shown in Figure 9(b).

In this experiment, radar echo data is collected from radar operating at X-band. The measurement is taken from 8 to 12 GHz in 20 MHz increments, HH polarization. The target viewing angles, relative to nose-on, ranged from $0°$ to $180°$ in $0.2°$ increments.

We assume that the target is illuminated by two collocated X-band wideband radars, simultaneously. Each radar operates at a different center frequency with 1 GHz bandwidth. The target viewing angle is $0 \sim 15°$. To simulate the amplitude and phase incoherence between multi-band data, the lower subband data is modulated by amplitude and phase ICP. After ICP estimation, PFA should be
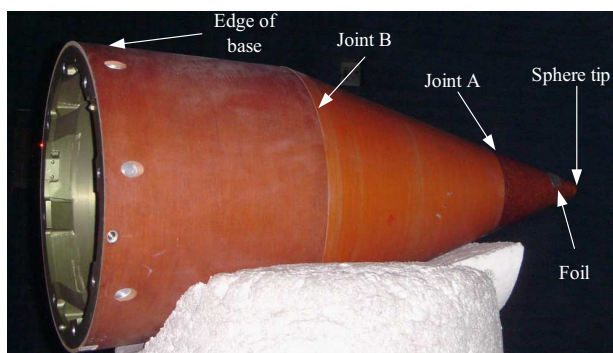

(a)
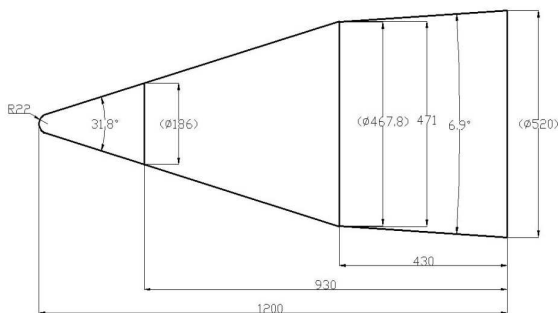
(b)

Figure 9. The shape and geometry of the blunt-nosed cone-cylinder target. (a) The shape of the target. (b) The geometry of the target.

applied to subbands before data fusion. Figures 10(a) and 10(b) show the lower and upper subband images, respectively. The resolution is insufficient to resolve subtle feature of important scattering centers, such as joint A and joint B, on the target along range direction. Compared to Figure 10(c), Figure 10(d) shows the image results by using 2-D GSSA without mutual-coherence, which cannot show the correct distribution of target scattering centers. As known, mutual-coherence must be done before data fusion. Figures 10(e)~(h) compare different fusion algorithms after mutual-coherence processing. Figure 10(e) shows the result of GAPES. As we can see, the method
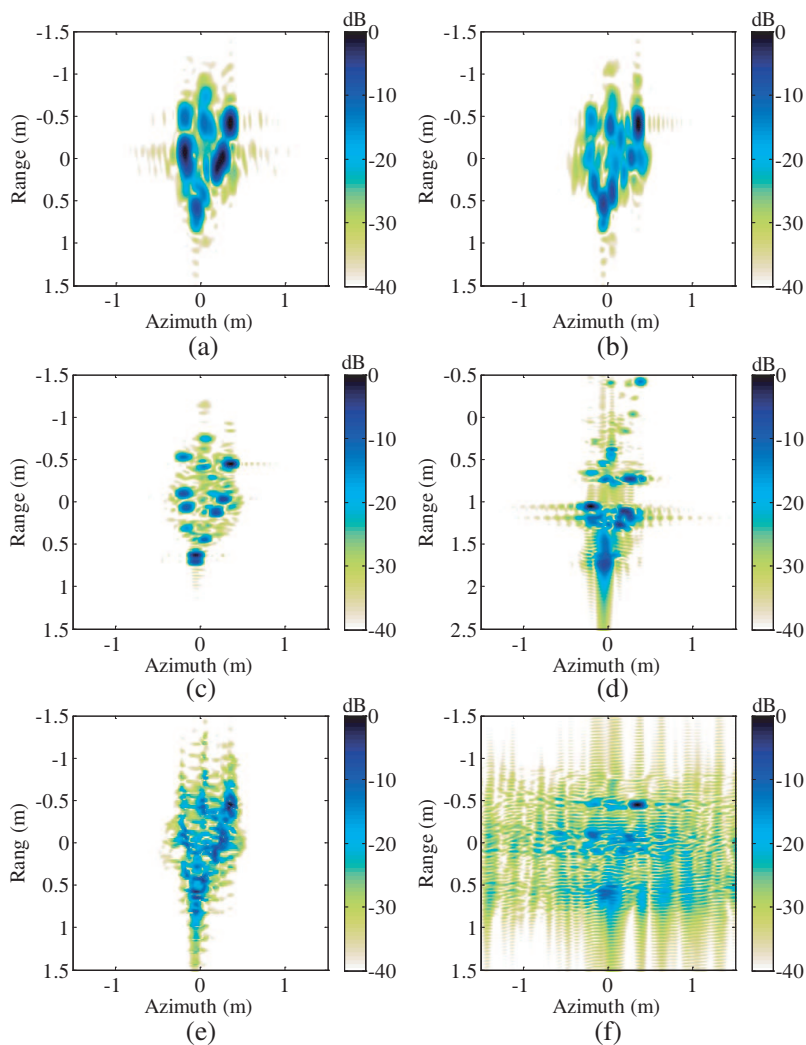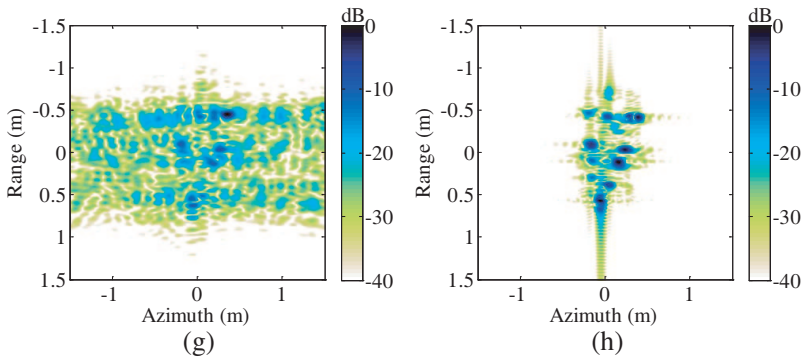
Figure 10. Comparison of 2-D radar images. (a) Subband (8.5 $\sim$ 9.5 GHz). (b) Subband (10.5 $\sim$ 11.5 GHz). (c) Full band (8 $\sim$ 12 GHz). (d) 2-D GSSA without mutual-coherence. (e) GAPES after mutual-coherence. (f) 1-D GSSA after mutual-coherence. (g) 1-D GSSA + MWN after mutual-coherence. (h) 2-D GSSA after mutual-coherence.

cannot improve range resolution, and target scattering centers are smeared. In the meanwhile, it needs huge time cost. Figures 10(f)$\sim$(g) show the results of 1-D GSSA and 1-D SSA combined with MWN, respectively. The target scattering centers are embedded in large amount of side lobes and fake scattering centers. As shown, 1-D method is not accurate enough to reconstruct target scattering centers. By using 2-D GSSA, we can obtain almost all the scattering centers information about the target, especially the joint A and joint B, edge of the base and high-order diffraction behind target base, as shown in Figure 10(h).

5. CONCLUSIONS

In this paper, we present a coherent processing method for distributed multi-band radar data to generate high-resolution images, in which DNCC algorithm and coherence function combined with statistical method are employed. Then, cohered subband signals are combined by 2-D GSSA method. The proposed method can be used to process multi-band data of different bandwidth and different gaps between them, which is verified by using a BNCCF target. The proposed data mutual-coherence method performs better than pole rotation method under different SNR levels. After data mutual-coherence process, 2-D GSSA exhibits better performance than GAPES, 1-D GSSA and 1-D SSA+MWN methods. The results validate the superiority of

this method. Apart from electromagnetic calculation data, a real target measured in microwave chamber is used to demonstrate the effectiveness of the proposed method.

REFERENCES

1. Cuomo, K. M., J. E. Piou, and J. T. Mayhan, "Ultrawide-band coherent processing," *IEEE Trans. Antennas Propag.*, Vol. 47, No. 6, 1094–1107, 1999.

2. Xu, X. J. and L. Jia, "Ultrawide-band radar imagery from multiple incoherent frequency subband measurements," *Journal of Systems Engineering and Electronics*, Vol. 22, No. 3, 398–404, 2011.

3. Liang, F. L., X. T. Huang, and P. Z. Lei, "A novel coherent algorithm of multiband radar echo," *Signal Processing*, Vol. 26, No. 6, 863–868, 2010.

4. Tian, J. H., J. P. Sun, G. H. Wang, Y. P. Wang, and W. X. Tan, "Multiband radar signal coherent fusion processing with IAA and apFFT," *IEEE Signal Process. Lett.*, Vol. 20, No. 5, 463–466, 2013.

5. Liu, C. L., F. He, and X. Z. Wei, "Research on multiple radar fusion imaging coherence compensation based on data correlation," *Systems Engineering and Electronics*, Vol. 32, No. 6, 1266–1271, 2010.

6. Li, H. J., N. H. Farhat, and Y. Shen, "A new iterative algorithm for extrapolation of data available in multiple restricted regions with application to radar imaging," *IEEE Trans. Antennas Propag.*, Vol. 35, No. 5, 581–588, 1987.

7. Cabrera, S. D. and T. W. Parks, "Extrapolation and spectral estimation with iterative weighted norm modification," *IEEE Trans. Signal Process.*, Vol. 39, No. 4, 842–851, 1991.

8. Wang, Q., R. B. Wu, M. D. Xing, and Z. Bao, "A new algorithm for sparse aperture interpolation," *IEEE Goesci. Remote Sensing Letters,* Vol. 4, No. 3, 480–484, 2007.

9. Larsson, E. G., P. Stoica, and J. Li, "Amplitude spectrum estimation for two-dimensional gapped data," *IEEE Trans. Signal Process.*, Vol. 50, No. 6, 1343–1354, 2002.

10. Larsson, E. G., G. Q. Liu, P. Stoica, and J. Li, "High-resolution SAR imaging with angular diversity," *IEEE Trans. Aerosp. Electron. Syst.*, Vol. 37, No. 4, 1359–1372, 2001.

11. Bai, X. R., F. Zhou, M. D. Xing, and Z. Bao, "High-resolution radar imaging of air targets from sparse azimuth data," *IEEE Trans. Aerosp. Electron. Syst.*, Vol. 48, No. 2, 1643–1655, 2012.

12. Piou, J. E., "A state-space technique for ultrawide-bandwidth coherent processing," Technical Report TR 1054, MIT Lincoln Laboratory, 1999.

13. Piou, J. E., "A state identification method for 1-D measurements with gaps," *AIAA Guidance Navigation and Control Conference*, 1–11, San Francisco, California, 2005.

14. Cetin, M. and W. C. Karl, "Feature-enhanced synthetic aperture radar image formation based on nonquadratic regularization," *IEEE Trans. Image Process.*, Vol. 10, No. 4, 623–631, 2001.

15. Cetin, M. and R. L. Moses, "SAR imaging from partial-aperture data with frequency-band omissions," *Proceedings of the SPIE Defense and Security Symposium*, Orlando, FL, 2005.

16. Mayhan, J. T., M. L. Burrows, K. M. Cuomo, and J. E. Piou, "High resolution 3D snapshot ISAR imaging and feature extraction," *IEEE Trans. Aerosp. Electron. Syst.*, Vol. 37, No. 2, 630–650, 2001.

17. Park, J.-I. and K.-T. Kim, "A comparative study on ISAR imaging algorithms for radar target identification," *Progress In Electromagnetics Research*, Vol. 108, 155–175, 2010.

18. Naishadham, K. and J. E. Piou, "A robust state space model for the characterization of extended returns in radar target signatures," *IEEE Trans. Antennas Propag.*, Vol. 56, No. 6, 1742–1751, 2008.

19. He, F. Y. and X. J. Xu, "A comparative study of two scattering center models," *IEEE 11th International Conference on Signal Processing*, 1931–1935, Beijing, 2012.

20. Akaike, H., "A new look at the statistical model identification," *IEEE Trans. Autom. Control.*, Vol. 19, No. 6, 716–723, 1974.

21. Wax, M. and T. Kailath, "Detection of signals by information theoretic criteria," *IEEE Trans. Acoust., Speech, Signal Process.*, Vol. 33, No. 2, 387–392, 1985.

22. Piou, J. E., "System realization using 2-D output measurements," *Proceedings of the 2004 American Control Conference*, 2840–2845, Boston, MA, USA, Jun. 2004.

23. Michaeli, A., "Equivalent edge currents for arbitrary aspects of observation," *IEEE Trans. Antennas Propag.*, Vol. 32, No. 3, 252–258, 1984.

24. Ausherman, D. A., A. Kozma, J. L. Walker, et al, "Developments in radar imaging," *IEEE Trans. Aerosp. Electron. Syst.*, Vol. 20, No. 4, 363–400, 1984.